







Unsplit superconducting and time reversal symmetry breaking transitions in Sr_2RuO_4 under hydrostatic pressure and disorder

Vadim Grinenko ^{1,2}✉, Debarchan Das ³, Ritu Gupta³, Bastian Zinkl⁴, Naoki Kikugawa⁵, Yoshiteru Maeno ⁶, Clifford W. Hicks ^{7,8}, Hans-Henning Klaus ¹, Manfred Sigrist⁴✉ & Rustem Khasanov ³✉

There is considerable evidence that the superconducting state of Sr_2RuO_4 breaks time reversal symmetry. In the experiments showing time reversal symmetry breaking, its onset temperature, T_{TRSB} , is generally found to match the critical temperature, T_c , within resolution. In combination with evidence for even parity, this result has led to consideration of a $d_{xz} \pm id_{yz}$ order parameter. The degeneracy of the two components of this order parameter is protected by symmetry, yielding $T_{\text{TRSB}} = T_c$, but it has a hard-to-explain horizontal line node at $k_z = 0$. Therefore, $s \pm id$ and $d \pm ig$ order parameters are also under consideration. These avoid the horizontal line node, but require tuning to obtain $T_{\text{TRSB}} \approx T_c$. To obtain evidence distinguishing these two possible scenarios (of symmetry-protected versus accidental degeneracy), we employ zero-field muon spin rotation/relaxation to study pure Sr_2RuO_4 under hydrostatic pressure, and $\text{Sr}_{1.98}\text{La}_{0.02}\text{RuO}_4$ at zero pressure. Both hydrostatic pressure and La substitution alter T_c without lifting the tetragonal lattice symmetry, so if the degeneracy is symmetry-protected, T_{TRSB} should track changes in T_c , while if it is accidental, these transition temperatures should generally separate. We observe T_{TRSB} to track T_c , supporting the hypothesis of $d_{xz} \pm id_{yz}$ order.

¹Institute for Solid State and Materials Physics, Technische Universität Dresden, Dresden, Germany. ²Leibniz-Institut für Festkörper- und Werkstofforschung (IFW) Dresden, Dresden, Germany. ³Laboratory for Muon Spin Spectroscopy, Paul Scherrer Institut, Villigen, Switzerland. ⁴Institute for Theoretical Physics, ETH Zurich, Zurich, Switzerland. ⁵National Institute for Materials Science, Tsukuba, Japan. ⁶Department of Physics, Kyoto University, Kyoto, Japan. ⁷Max Planck Institute for Chemical Physics of Solids, Dresden, Germany. ⁸School of Physics and Astronomy, University of Birmingham, Birmingham, UK.
✉email: vadim.a.grinenko@gmail.com; mansigri@ethz.ch; rustem.khasanov@psi.ch

For unconventional superconductors identifying the symmetry of the order parameter is crucial to pinpoint the origin of the superconductivity. Unconventional pairing states are distinguished from conventional ones by a non-trivial intrinsic phase structure which causes additional spontaneous symmetry breaking at the superconducting phase transition. This can lead, for instance, to a reduction of the crystal symmetry or the loss of time reversal symmetry. Indeed, several superconductors are known, which show experimental responses consistent with time reversal symmetry breaking (TRSB) superconductivity^{1–11}.

TRSB superconducting states are formed by combining two or more order parameter components with complex coefficients. These components may be degenerate by symmetry, belonging to a single irreducible representation of the crystalline point group (as in the case of $p_x \pm ip_y$ or $d_{xz} \pm id_{yz}$ superconductivity on a tetragonal lattice), or they may come from different representations (for example, $d_{xy} \pm id_{x^2-y^2}$ superconductivity on a tetragonal lattice). In the following, we refer to the former as single-representation and the latter as composite-representation order parameters. For composite-representation order parameters, the two components will generally onset at different temperatures. The higher transition temperature becomes T_c , the superconducting critical temperature, and the lower temperature T_{TRSB} , the temperature where TRSB onsets. The possibility of composite order parameters is usually dismissed out of hand, because it is unusual for two components that are not related by symmetry to be close enough in energy. However, there are a few known examples: s and $d_{x^2-y^2}$ are relatively close in energy in iron-based superconductors^{11,12}, while both (U,Th)Be₁₃^{1,4} and UPt₃^{2,3,8} have split T_c and T_{TRSB} .

Here, we study Sr₂RuO₄, an unconventional superconductor^{13,14}, in which the origin of the superconductivity remains a mystery. Evidence that this superconductor breaks time reversal symmetry comes from zero-field muon spin rotation/relaxation (ZF- μ SR) experiments¹⁵ and polar Kerr effect measurements¹⁶. Phase-sensitive probes using a corner SQUID device give further support¹⁷. Moreover, the Josephson effect between a conventional superconductor and Sr₂RuO₄ reveal features compatible with the presence of superconducting domains, as expected for TRSB superconductivity^{18–20}. For two decades, the leading candidate state to explain these and other observations was the chiral p -wave state $p_x \pm ip_y$ (the lattice symmetry of Sr₂RuO₄ is tetragonal), which has odd parity and therefore equal spin pairing. However, there is compelling evidence against an order parameter with such spin structure. This evidence includes paramagnetic limiting for in-plane magnetic fields^{21–23} and the recently discovered drop in the NMR Knight shift below T_c ^{24,25}. In combination with the above experimental support for TRSB superconductivity, this evidence compels consideration of $d_{xz} \pm id_{yz}$ order.

$d_{xz} \pm id_{yz}$ order would be a surprise because it has a line node at $k_z = 0$, which under conventional understanding requires inter-layer pairing, while in Sr₂RuO₄ interlayer coupling is very weak. It has been proposed that $d_{xz} \pm id_{yz}$ order might be obtained through multi-orbital degrees of freedom; in this model the order parameter symmetry is encoded in orbital degrees of freedom, so interlayer pairing is not required²⁶. This form of pairing is also under consideration for URu₂Si₂^{27,28}. However, so far it has not been unambiguously confirmed in any material. To avoid horizontal line nodes, the composite-representation order parameters $s \pm id_{x^2-y^2}$ ²⁹, $s \pm id_{xy}$ ³⁰ and $d_{x^2-y^2} \pm ig_{xy(x^2-y^2)}$ ^{31,32} have also recently been proposed for Sr₂RuO₄. In contrast to $d_{xz} \pm id_{yz}$, these require tuning to obtain $T_c \approx T_{\text{TRSB}}$ on a tetragonal lattice.

In this work, to test whether the order parameter of Sr₂RuO₄ is of single- or composite-representation type we perform ZF- μ SR

measurements on hydrostatically pressurised Sr₂RuO₄ and on La-doped Sr_{2-y}La_yRuO₄. Both of these perturbations maintain the tetragonal symmetry of the lattice. If the order parameter has single-representation nature, T_{TRSB} will track T_c . If the order parameter is of the composite-representation kind, with T_{TRSB} matching T_c in clean, unstressed samples through an accidental fine tuning, then perturbations away from this point should in general split T_{TRSB} and T_c , whether they preserve tetragonal lattice symmetry or not³³. Here, we have observed a clear suppression of T_{TRSB} at a rate matching the suppression of T_c . Our experimental results provide evidence in favour of single-representation nature of the order parameter in Sr₂RuO₄.

Results

μ SR on Sr₂RuO₄ under hydrostatic pressure. The hydrostatic pressure measurement setup is shown schematically in Fig. 1. Sr₂RuO₄ crystals of diameter $\varnothing \sim 3$ mm were affixed to oxygen-free copper foils, and assembled into an approximately cylindrical collection of total diameter $\varnothing \sim 7$ mm and total length $l \sim 12$ mm (see Fig. 1a). The c -axes of the separate crystals were aligned to within 3°.

The pressure cell used in the present study (refs. 34,35 and Fig. 1b) is a modification of a “classic μ SR” clamped pressure cell^{35,36}. It consists of a main body that encloses the sample and pressure medium, a teflon cap with a metallic support, a tungsten carbide piston, a pressing pad and a clamping bolt (not shown) that holds the piston in place. All the metallic parts of the cell apart from the piston are made from a nonmagnetic beryllium-copper alloy, which is known to have a temperature-independent μ SR response^{34–36}. The main feature of this cell is that the only materials placed in the muon beam are the sample, the pressure medium and this CuBe alloy. The muons had a typical momentum of 97 MeV/c, sufficient to penetrate the walls of the pressure cell. The pressure medium was 7373 Daphne oil, which at room temperature solidifies at a pressure $p \approx 2.3$ GPa³⁷. The maximum pressure reached here was 0.95 GPa, and therefore hydrostatic conditions are expected. The pressure was determined by monitoring the critical temperature of a small piece of indium (the pressure indicator) placed inside the cell with the Sr₂RuO₄ sample. Confirmation that essentially hydrostatic conditions were attained is provided by the fact that T_c was observed to decrease linearly with pressure, whereas in-plane uniaxial stress on a GPa scale causes a strong non-linear increase in T_c ³⁸.

The samples used here were grown by the standard floating zone method³⁹. Measurements of heat capacity of pieces cut from the ends of the rods used here revealed an average T_c of 1.30(6) K (see Supplementary Fig. 1 in Supplementary Note 1), slightly below the limit of T_c of 1.50 K for a pure sample.

T_c and T_{TRSB} were both obtained by means of μ SR, ensuring that both quantities were measured for precisely the same sample volume. In the μ SR method, spin-polarised muons are implanted, and their spins then precess in the local magnetic field. By collecting statistics of decay positrons in selected direction(s), the muon polarisation as a function of time after implantation, $P_\mu(t)$, can be determined; the time-evolution of this polarisation is determined by the magnetic fields in the sample⁴⁰.

T_c is determined through transverse-field (TF) measurements. An external field B_{ext} of 3 mT, as is generated by Helmholtz coils, was applied parallel to the crystalline c -axis and perpendicular to the initial muon spin polarisation $\mathbf{P}_\mu(0)$. Measurements were performed in the field-cooled (FC) mode. Details of the method and analysis are given in the “Methods” section.

Example TF- μ SR time spectra at pressure $p = 0.95$ GPa, and at a temperature above T_c and one below, are shown in Fig. 2a. Above T_c , the spins of muons stopped in both the sample and the

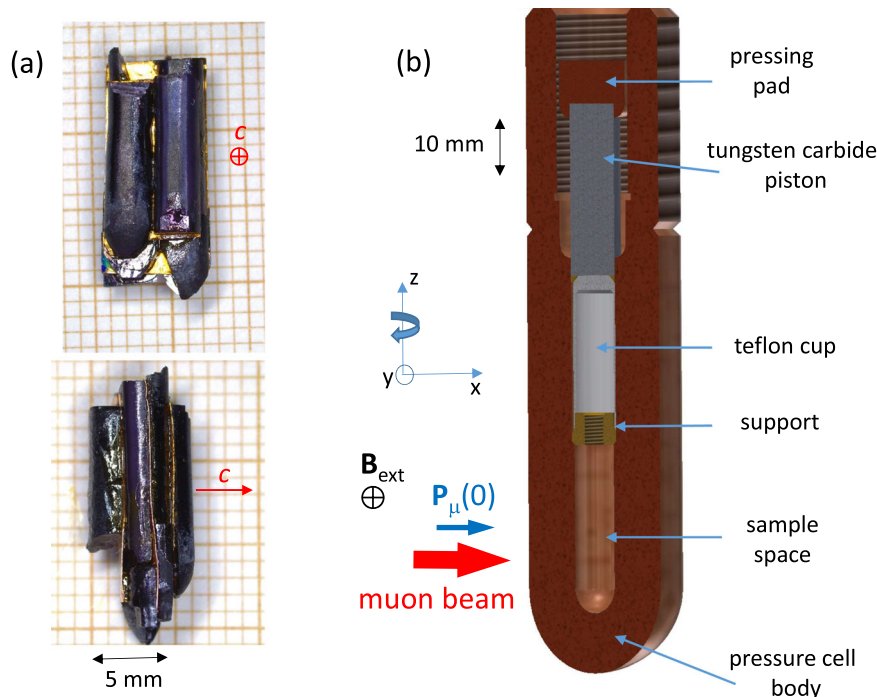


Fig. 1 Setup for hydrostatic pressure experiments. **a** Sr_2RuO_4 sample, consisting of semi-cylindrical pieces glued on oxygen-free copper foils. The top and the bottom panels are the front and the side view, respectively. The crossed circle and the arrow indicate the orientation of the c -axis. **b** Construction of the pressure cell³⁴. The sample and the pressure medium are surrounded only by beryllium-copper (the pressure cell body and the teflon cap support). The parts of the cell with strong μSR response (teflon cap and tungsten carbide piston) are far from the sample and outside of the muon beam. The initial muon spin polarisation $\mathbf{P}_\mu(0)$ and the external field \mathbf{B}_{ext} in TF- μSR measurements are aligned along the x - and y -axes, respectively. By rotating the cell about the z -axis, the angle between $\mathbf{P}_\mu(0)$ and the sample c -axis can be varied.

pressure cell walls precess with frequency $\omega = \gamma_\mu B_{\text{ext}}$ (where $\gamma_\mu = 2\pi \times 135.5$ MHz/T is the muon gyromagnetic ratio). The muon spin polarisation is seen to relax substantially on a $10 \mu\text{s}$ time scale. This is because $\sim 50\%$ of muons are implanted into the CuBe, where the nuclear magnetic moments of Cu rapidly relax their polarisation. Below T_c , the internal field in the sample becomes highly inhomogeneous due to the appearance of a flux-line lattice, and so the polarisation of the muons that implanted in the sample also relaxes quickly.

TF- μSR measurements were performed at 0, 0.25, 0.62, and 0.95 GPa. Data at 0 and 0.95 GPa are shown in Fig. 2, and at the other two pressures in Supplementary Figs. 3 and 4 in Supplementary Note 2. Data are analysed as a sum of background and sample contributions, given by Eqs. (3) and (4) (in the “Methods” section), respectively. From the sample contribution we extract a Gaussian relaxation rate, σ , and the diamagnetic shift of the field inside the sample, $B_{\text{int}} - B_{\text{ext}} \propto M_{\text{FC}}$ ⁴¹ (M_{FC} is the FC magnetisation). Figure 2b, c, respectively, shows the temperature dependence of σ and $B_{\text{int}} - B_{\text{ext}}$. σ is given by $\sigma^2 = \sigma_{\text{sc}}^2 + \sigma_{\text{nm}}^2$, where σ_{sc} and σ_{nm} are the flux-line lattice and nuclear moment contributions, respectively. $\sigma_{\text{sc}} \propto \lambda_{\text{ab}}^{-2}$, where λ_{ab} is the in-plane magnetic penetration depth; see ref. ⁴² and the “Methods” section. The onset of superconductivity can be seen in both σ and $B_{\text{int}} - B_{\text{ext}}$, as a transition rounded on a scale of ~ 0.1 K. The heat capacity measurements show a similar distribution of T_c 's; see Supplementary Fig. 1 in Supplementary Note 1.

The pressure dependence of T_c is shown in Fig. 2g. The error bars in the figure are the rounding on the transition, and can be taken as an absolute error on T_c . When fitting $\sigma(T)$ and $B_{\text{int}}(T)$ with model functions, the statistical error on the T_c 's extracted is considerably smaller, meaning that the error on changes in T_c is low. A linear fit to $T_c(p)$ yields a slope $dT_c/dp = -0.24(2)$ K/GPa,

which is in good agreement with literature data^{43–45}. The unpressurised T_c is found to be 1.26(5) K, in good agreement with 1.30(6) K found in the heat capacity measurements, see Supplementary Note 1.

T_{TRSB} is determined through ZF measurements. The signature of TRSB is an enhancement in the muon spin relaxation rate below T_{TRSB} , indicating the appearance of spontaneous magnetic fields. In these measurements, external fields were compensated to better than $2 \mu\text{T}$, ruling out flux lines below T_c as the origin of this signal. An example of ZF- μSR time spectra above and below T_c , showing the faster relaxation below T_c , at $p = 0.95$ GPa is presented in Fig. 2d. The pressure cell background is T -independent, so the increased signal decay comes from the sample. The sample contribution was modelled by a two-component relaxation function: $\text{GKT}(t) \cdot \exp(-\lambda t)$, in accordance with the results of refs. ^{5,6,9,15,46,47}; see also the “Methods” section. Here, $\text{GKT}(t)$ is the Gaussian Kubo-Toyabe function describing the relaxation of muon spin polarisation in the random magnetic field distribution created by nuclear magnetic moments, and $\exp(-\lambda t)$ is a Lorentzian decay function accounting for appearance of spontaneous magnetic fields. Temperature dependencies of the exponential relaxation rate, λ , at 0 and 0.95 GPa, for independent measurements with the initial muon spin polarisation $\mathbf{P}_\mu(0) \parallel c$ and $\parallel ab$, are shown in Fig. 2e, f; ZF data at 0.25 and 0.62 GPa are shown in Supplementary Figs. 3 and 4 in Supplementary Note 2.

To extract T_{TRSB} , $\lambda(T)$ is fitted with the following functional form:

$$\lambda(T) = \begin{cases} \lambda_0, & T > T_{\text{TRSB}} \\ \lambda_0 + \Delta\lambda \left[1 - \left(\frac{T}{T_{\text{TRSB}}} \right)^n \right], & T < T_{\text{TRSB}}. \end{cases} \quad (1)$$

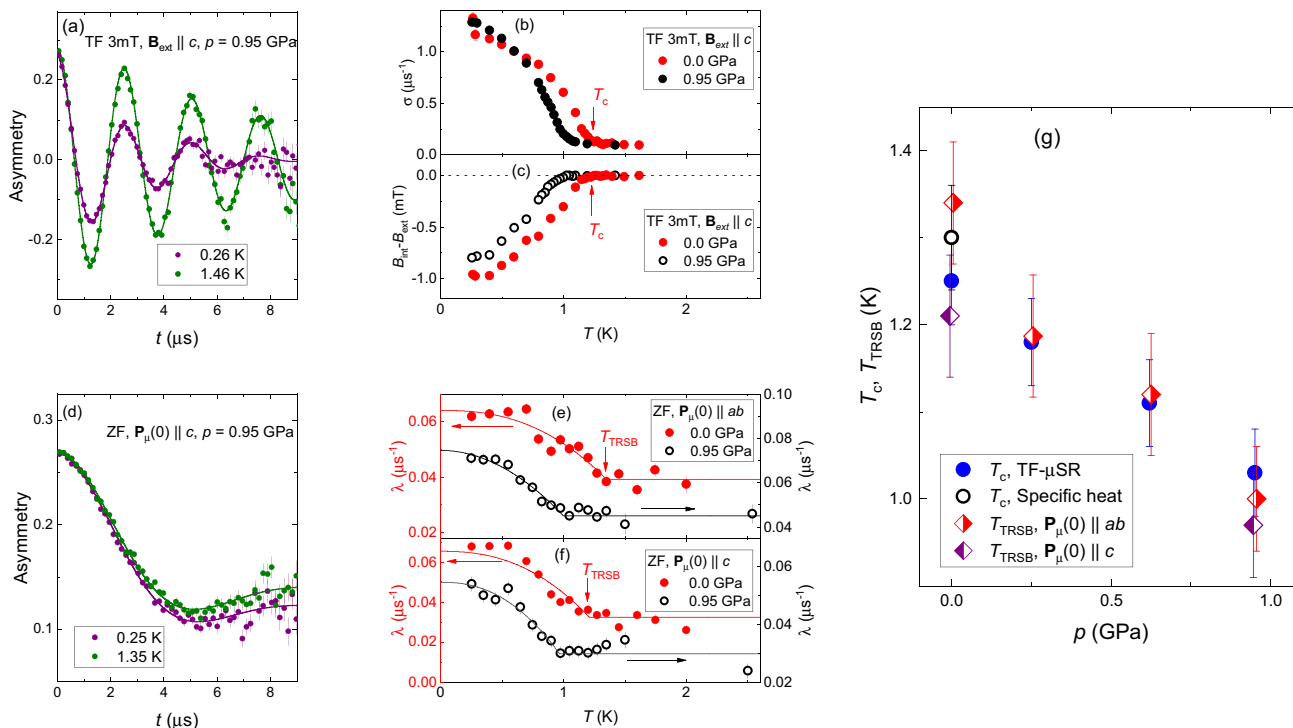


Fig. 2 Effect of pressure on T_c and T_{TRSB} in Sr_2RuO_4 . **a** TF- μSR time-spectra above and below T_c measured at $p = 0.95$ GPa and $B_{\text{ext}} = 3$ mT, with $\mathbf{B}_{\text{ext}} \parallel c$. The plotted quantity is the detection asymmetry between two positron detectors, which is proportional to the muon spin polarisation $P_\mu(t)$. The solid lines are fits of Eq. (2), with the sample and the pressure cell contributions described by Eqs. (3) and (4), respectively. **b, c** Temperature dependencies of the Gaussian relaxation rate σ and the diamagnetic shift $B_{\text{int}} - B_{\text{ext}} \propto M_{\text{FC}}$ at $p = 0.0$ and 0.95 GPa. Arrows indicate the position of the superconducting transition temperature T_c at $p = 0.0$ GPa. **d** ZF- μSR time-spectra above and below T_c , measured at $p = 0.95$ GPa and with initial muon spin polarisation $\mathbf{P}_\mu(0) \parallel c$. The solid lines are fits of Eq. (2), with the sample and the pressure cell parts described by Eqs. (5) and (7). **e, f** Temperature dependencies of the ZF exponential muon spin relaxation rate λ at $p = 0.0$ and 0.95 GPa. In **e**, $\mathbf{P}_\mu(0) \parallel ab$, and in **f**, $\mathbf{P}_\mu(0) \parallel c$. The solid lines are fits of Eq. (1) to the data. Arrows indicate the position of T_{TRSB} at $p = 0.0$ GPa. **g** Dependence of T_c and T_{TRSB} on pressure. Open circle correspond to an average T_c of $1.30(6)$ K determined from specific heat data (see Supplementary Fig. 1 in Supplementary Note 1). The displayed error bars for μSR data correspond to one standard deviation from the χ^2 fit⁷¹. The displayed error bars for T_c indicate the rounding of the transition on a scale of approximately 0.1 K. The error bars for μSR data and T_{TRSB} correspond to one standard deviation from the χ^2 fit⁷¹.

λ_0 is the relaxation rate above T_{TRSB} , and $\Delta\lambda$ is the enhancement due to spontaneous magnetic fields. Where data were obtained both for $\mathbf{P}_\mu(0) \parallel c$ and $\parallel ab$, the exponent n is constrained to be the same for both polarisations. T_{TRSB} , λ_0 , and $\Delta\lambda$ were obtained independently for each pressure and muon spin polarisation. The resulting values of T_{TRSB} are plotted in Fig. 2g.

Our ZF data yield the following three results:

- (1) Where data were taken both for $\mathbf{P}_\mu(0) \parallel c$ and $\parallel ab$ (that is, at 0 and 0.95 GPa), T_{TRSB} and $\Delta\lambda$ were found to be the same within resolution for both polarisations. [At 0 GPa, $\Delta\lambda = 0.027(4)$ and $0.033(3) \mu\text{s}^{-1}$, and at 0.95 GPa, $0.030(4)$ and $0.025(3) \mu\text{s}^{-1}$, for $\mathbf{P}_\mu(0) \parallel ab$ and $\mathbf{P}_\mu(0) \parallel c$, respectively.] This agrees with the zero-pressure results of Luke et al.¹⁵. Because $\Delta\lambda$ reflects fields perpendicular to $\mathbf{P}_\mu(0)$, this result indicates that the spontaneous fields have no preferred orientation.
- (2) $\Delta\lambda$ was found to be pressure-independent within resolution (including all pressures investigated: 0, 0.25, 0.62 and 0.95 GPa), having an average value of $\Delta\lambda = 0.026(2) \mu\text{s}^{-1}$. This value corresponds to a characteristic field strength $B_{\text{TRSB}} = \Delta\lambda/\gamma_\mu = 0.031(2)$ mT. B_{TRSB} has been found to vary from sample to sample⁴⁷, and this value is in line with previous reports (see refs. 15,46,48,49 and Table 1).

- (3) A linear fit yields $T_{\text{TRSB}}(p) = 1.27(3) \text{ K} - p \cdot 0.29(5) \text{ K/GPa}$. In other words, within resolution the rate of suppression of T_{TRSB} under hydrostatic pressure matches that of T_c .

μSR on $\text{Sr}_{1.98}\text{La}_{0.02}\text{RuO}_4$. Substitution of La for Sr adds electrons to the Fermi surfaces; in $\text{Sr}_{2-y}\text{La}_y\text{RuO}_4$ this doping drives the largest Fermi surface through a Lifshitz transition from an electron-like to a hole-like geometry, at $y \approx 0.20$ ^{50,51}. At $y = 0.02$, the change in Fermi surface structure is minimal, and the main effect of the La-substitution is to suppress T_c , through the added disorder. Heat capacity data, measured on a small piece cut from the μSR sample, give $T_c = 0.70(5)$ K, where the error reflects the width of the transition (see Supplementary Fig. 2 in Supplementary Note 1).

This sample was studied at zero pressure. With no pressure cell material in the beam, the background is much smaller. The typical muon momentum was $28 \text{ MeV}/c$, giving of ~ 0.2 mm implantation depth⁴⁰. Representative TF- μSR time spectra above and below T_c , where the applied field is $B_{\text{ext}} = 2$ mT parallel to the crystalline c -axis, are shown in Fig. 3a. Below T_c , the muon spin polarisation relaxes almost completely on a $10 \mu\text{s}$ time scale, showing that essentially the entire sample volume is superconducting. The TF Gaussian relaxation rate σ is shown in Fig. 3b, and $B_{\text{int}} - B_{\text{ext}}$ in Fig. 3c. These measurements yield $T_c = 0.75(5)$ K. The heat capacity data are also shown in Fig. 3b.

Table 1 Enhancement of the exponential relaxation rates $\Delta\lambda$ and corresponding values of the spontaneous magnetic fields $B_{\text{TRSB}} = \Delta\lambda/\gamma_\mu$ caused by formation of TRSB state in Sr_2RuO_4 and related compounds.

	T_c (K)	$\Delta\lambda$ (μs^{-1})	B_{TRSB} (mT)	Reference
Sr_2RuO_4 (0.0 GPa)	1.26 (5)	0.030 (3)	0.025 (3)	This study
Sr_2RuO_4 (0.25 GPa)	1.18 (5)	0.024 (3)	0.021 (3)	This study
Sr_2RuO_4 (0.62 GPa)	1.11 (5)	0.024 (3)	0.021 (3)	This study
Sr_2RuO_4 (0.95 GPa)	1.03 (5)	0.028 (3)	0.024 (3)	This study
$\text{Sr}_{1.98}\text{La}_{0.02}\text{RuO}_4$	0.75 (5)	0.007 (1)	0.006 (1)	This study
Sr_2RuO_4	≈ 1.45	≈ 0.037	≈ 0.032	ref. 15
Sr_2RuO_4	≈ 1.45	≈ 0.029	≈ 0.025	ref. 46
Sr_2RuO_4	≈ 1.1	≈ 0.035	≈ 0.030	ref. 46
Sr_2RuO_4	-1.5	≈ 0.041	≈ 0.035	ref. 48
$\text{Sr}_2\text{RuO}_4\text{-Ru}$	-1.5	≈ 0.073	≈ 0.062	ref. 48
$\text{Sr}_3\text{Ru}_2\text{O}_7$	-2.5	≈ 0.038	≈ 0.033	ref. 48
Sr_2RuO_4	≈ 1.45	≈ 0.020	≈ 0.017	ref. 49
Sr_2RuO_4	1.38 (4)	0.0088 (10)	0.0075 (9)	ref. 47
Sr_2RuO_4	1.22 (6)	0.024 (2)	0.020 (2)	ref. 47

Only the experiments with preserved tetragonal lattice symmetry resulting in $T_c \approx T_{\text{TRSB}}$ are considered. In a case when the results of both, $\mathbf{P}_\mu(0)\parallel c$ and $\mathbf{P}_\mu(0)\parallel ab$ experiments are available (present study and ref. 15), the values of $\Delta\lambda$ are averaged out.

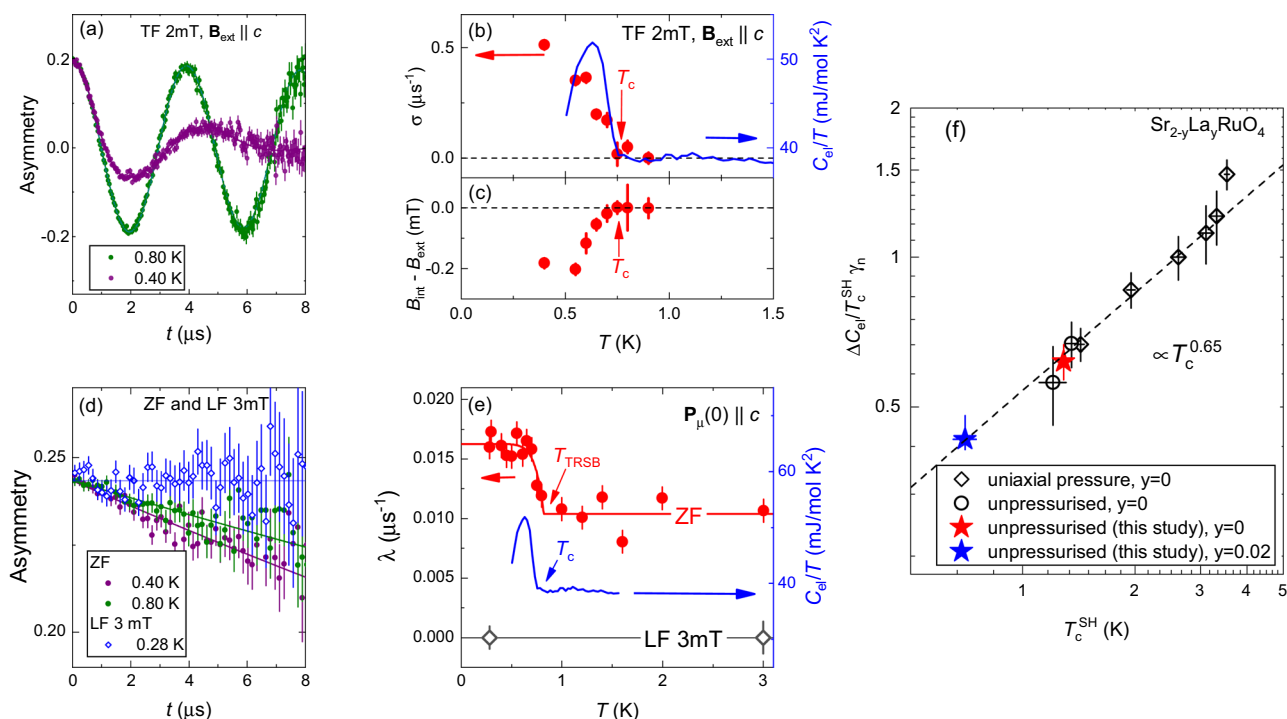


Fig. 3 TRSB in $\text{Sr}_{1.98}\text{La}_{0.02}\text{RuO}_4$. **a** TF- μ SR time-spectra above and below T_c measured at $B_{\text{ext}} = 2$ mT with $\mathbf{B}_{\text{ext}}\parallel c$. The solid lines are fits of Eq. (3) to the data. **b, c** Temperature dependencies of the Gaussian relaxation rate σ and the diamagnetic shift $B_{\text{int}} - B_{\text{ext}}$, respectively. Arrows indicate the superconducting transition temperature T_c , determined from the TF- μ SR data. The blue curve in **b** is the electronic specific heat C_{el}/T , measured on a small piece cut from the μ SR sample. **d** ZF- and LF- μ SR time-spectra. ZF data from above and below T_c , measured with $\mathbf{P}_\mu(0)\parallel c$, are shown. The LF data are from T well below T_c and with $\mathbf{B}_{\text{ext}} = 3$ mT $\parallel \mathbf{P}_\mu(0)$. The solid lines are fits of Eq. (8). **e** Temperature dependence of the ZF and LF exponential relaxation rate λ . The solid red line is the fit of Eq. (1) to ZF $\lambda(T)$ data. The blue curve is, again, C_{el}/T . Arrows indicate positions of T_c and T_{TRSB} . **f** Double logarithmic plot of the normalised specific heat jump $\Delta C_{\text{el}}/\gamma_n T_c^{\text{SH}}$ versus T_c^{SH} [γ_n is the Sommerfeld coefficient and T_c^{SH} is the transition temperature determined from $C_{\text{el}}/T(T)$ by means of equal-entropy construction, see Supplementary Fig. 1 in Supplementary Note 1]. Values of $\Delta C_{\text{el}}/\gamma_n T_c^{\text{SH}}$ are determined in a way presented in Supplementary Fig. 2 in Supplementary Note 1. Filled symbols: data from this work; open symbols: data taken from refs. 47,52. The displayed error bars for μ SR data correspond to one standard deviation from the χ^2 fit⁷¹. The error bars for $\Delta C_{\text{el}}/\gamma_n T_c^{\text{SH}}$ and T_c^{SH} indicate uncertainty in selecting the temperature range for linear fit below T_c .

ZF- μ SR data are presented in Fig. 3d, e. Fitting with Eq. (1) returns $\Delta\lambda = 0.007(1) \mu\text{s}^{-1}$ and $T_{\text{TRSB}} = 0.8(1)$ K. This $\Delta\lambda$ is noticeably smaller than that obtained from the undoped Sr_2RuO_4 sample, corresponding to an internal field $B_{\text{TRSB}} \approx 0.01$ mT. It is,

however, within the range of previous results⁴⁷. In qualitative agreement with data on a lower T_c Sr_2RuO_4 , reported in ref. 46, though here with more data at $T > T_c$ to be certain of the base relaxation rate, this low value of $\Delta\lambda$ shows that B_{TRSB} is not

straightforwardly related to defect density. At present, the origin of the sample-to-sample variation in B_{TRSB} is unknown.

Longitudinal-field (LF) measurements can be employed to determine whether internal fields are static or fluctuating. If B_{TRSB} is static, under an applied field parallel to $\mathbf{P}_\mu(0)$ that is considerably larger than B_{TRSB} , muon spin precession is greatly restricted and the spin polarisation does not relax (i.e. the muon spins decouple from B_{TRSB}). In contrast, fluctuating B_{TRSB} can still relax the muon spin polarisation⁴⁰. Data shown in Fig. 3d, e indicate that $\mathbf{B}_{\text{ext}} \parallel \mathbf{P}_\mu(0) = 3$ mT fully suppresses the muon spin relaxation, and therefore that B_{TRSB} is static on a microsecond time scale, in agreement with data on clean Sr_2RuO_4 reported in ref. 15. We note that LF measurements were not performed on the hydrostatically pressurised sample because the decoupling field for the Cu background is of the order of 10 mT, considerably stronger than that for Sr_2RuO_4 .

Heat capacity measurements. The specific heat measurements were performed at ambient pressure for several pieces of $\text{Sr}_{2-y}\text{La}_y\text{RuO}_4$ single crystals. The results are presented in Fig. 3b, e for $\text{Sr}_{1.98}\text{La}_{0.02}\text{RuO}_4$ ($y = 0.02$) and in Supplementary Fig. 1 in Supplementary Note 1 for Sr_2RuO_4 ($y = 0.0$), respectively. The specific heat jumps at T_c ($\Delta C_{\text{el}}/\gamma_n T_c$, γ_n is the Sommerfeld coefficient) were further obtained in a way presented in Supplementary Fig. 2 in Supplementary Note 1.

Figure 3f summarises the $\Delta C_{\text{el}}/\gamma_n T_c^{\text{SH}}$ vs. T_c^{SH} data for our $\text{Sr}_{2-y}\text{La}_y\text{RuO}_4$ samples. Here T_c^{SH} denotes the superconducting transition temperature determined from C_{el}/T vs. T measurement curves by means of equal-entropy construction algorithm, see Supplementary Fig. 1a in Supplementary Note 1. In addition, we have also included some literature data for Sr_2RuO_4 with different amount of disorder⁴⁷, and for Sr_2RuO_4 under uniaxial strain⁵². In total, Fig. 3f compares Sr_2RuO_4 samples with a factor of five variation in T_c . Remarkably, $\Delta C_{\text{el}}/\gamma_n T_c$ vs. T_c data points scale as T_c^α with $\alpha \approx 0.65$, which is distinctly different from the BCS behaviour, where $\alpha = 0$ ($\Delta C_{\text{el}}/\gamma_n T_c = \text{const}$). Just a single point at $T_c \approx 3.5$ K deviates from the scaling behaviour, which might be associated with tuning the electronic structure of Sr_2RuO_4 close to a van Hove singularity⁵². The results presented in Fig. 3f indicate, therefore, that the perturbation changes the gap structure on the Fermi surface, i.e. its “anisotropy” or the distribution among the three different bands which can lead to a renormalisation of the specific heat jump being not simply proportional to the normal-state-specific heat above T_c .

Such scaling behaviour is rarely observed since the ratio $\Delta C_{\text{el}}/\gamma_n T_c$ is sensitive to a change of the superconducting gap structure and symmetry. Note that a similar scaling is reported for Fe-based superconductors, where $\Delta C_{\text{el}}/\gamma_n T_c$ follows approximately the BNC (Bud’ko-Ni-Canfield) scaling behaviour $\Delta C_{\text{el}}/\gamma_n T_c \propto T_c^\alpha$ with $\alpha \approx 2.53$, which is considered to be a consequence of the unconventional multiband $s \pm$ superconductivity. The change of the superconducting pairing state in the $\text{Ba}_{1-x}\text{K}_x\text{Fe}_2\text{As}_2$ system results in abrupt change of the scaling behaviour leading to an intermediate $s + is$ state¹¹. The monotonic $\Delta C_{\text{el}}/\gamma_n T_c$ vs. T_c behaviour obtained in the present study suggests, therefore, that La-substitution do not yield a change of the superconducting gap symmetry. Consequently, the superconducting gap structure does not undergo a significant change due to effects of disorder and it remains the same as in bare Sr_2RuO_4 compound.

Discussion

In a previous ZF- μ SR experiment, in-plane uniaxial pressure, which does lift the tetragonal symmetry of the unpressurised lattice, was found to induce a strong splitting between T_c and T_{TRSB} ⁴⁷. Uniaxial pressure drives a strong increase in T_c , while

T_{TRSB} varies much more weakly, probably decreasing slightly with initial application of pressure. The microscopic mechanism yielding the signal observed at T_{TRSB} , a weak enhancement in muon spin relaxation rate, remains unclear: the main proposed mechanism, magnetism induced at defects and domain walls by a TRSB superconducting order, is unproved experimentally^{54,55}. At present, the link between enhanced muon spin relaxation and TRSB superconductivity is, therefore, mainly empirical, based on: (1) the facts that it is a signal seen in only a small fraction of known superconductors, (2) it generally appears at T_c and (3) the general notion that TRSB superconductivity can in principle generate magnetic fields, while muons detect magnetic fields. In ref. 47, careful checks were performed to rule out instrumentation artefact as the origin of the signal at T_{TRSB} , and it was further argued that this signal is extremely difficult to obtain from a purely magnetic mechanism. Nevertheless, the weak observed variation of T_{TRSB} , while T_c varied strongly, raised some doubt as to whether this signal is in fact associated with the superconductivity.

Here, we have observed a clear suppression of T_{TRSB} with hydrostatic stress, at a rate matching the suppression of T_c . This result further strengthens the evidence that enhanced muon spin relaxation is an indicator of TRSB superconductivity: T_{TRSB} tracks T_c when tetragonal lattice symmetry is preserved, while the splitting induced by uniaxial pressure shows unambiguously that it is a distinct transition, and not an artefact through some unidentified mechanism of the superconducting transition itself. Figure 4 shows T_{TRSB} versus T_c . The data reported here, on hydrostatically pressurised Sr_2RuO_4 and on unpressurised $\text{Sr}_{1.98}\text{La}_{0.02}\text{RuO}_4$, fall on the $T_{\text{TRSB}} = T_c$ line, while the uniaxial pressure data from ref. 47 clearly deviate from this line.

Our central finding that T_{TRSB} tracks T_c provides further support for the single-representation $d_{xz} \pm id_{yz}$ order parameter. Importantly, homogeneous $d_{xz} \pm id_{yz}$ is the only spin-singlet order parameter consistent with the selection rules imposed by ultrasound and Kerr effect data. Ultrasound data on Sr_2RuO_4 ^{56,57} show a type of renormalisation that is not possible for a single-component order parameter on a tetragonal lattice: a jump in ultrasound velocity at T_c for transverse modes. While these experimental results are not sensitive to the spin configuration, they impose other stringent conditions on the possible pairing symmetries^{58,59}. The polar Kerr effect mentioned above is a second experiment which provides symmetry-related constraints, being compatible only with chiral pairing states¹⁶. These two selection rules are obeyed by both the chiral p -wave and chiral d -wave state, though as noted in the Introduction, p -wave order appears to be ruled out by NMR Knight shift data^{24,25}. In contrast, the composite-representation states do not satisfy the requirements for both selection rules. The $d_{x^2-y^2} + ig_{xy(x^2-y^2)}$ and $s + id_{xy}$ states are constructed to be compatible with the ultrasound measurements, but they are not chiral^{31,60}. The $s + id_{x^2-y^2}$ state violates both selection rules²⁹. It can be generally stated that any composite-representation pairing states in a tetragonal crystal, composed of components of two one-dimensional representations, would satisfy at most one of the two selection rules (see the “Methods” section).

We note that there is a recent proposal for inhomogeneous superconductivity in Sr_2RuO_4 : single-component ($d_{x^2-y^2}$) in the bulk, but two-component ($d_{x^2-y^2} + ig_{xy(x^2-y^2)}$) in the strain fields around dislocations⁶¹. The combination of phase locking between adjacent dislocations and a preferred orientation to the dislocations would result in a bulk chirality. In this proposal, T_{TRSB} could be locked to T_c by hypothesising that superconductivity appears at the dislocations before the bulk, but tuning would then

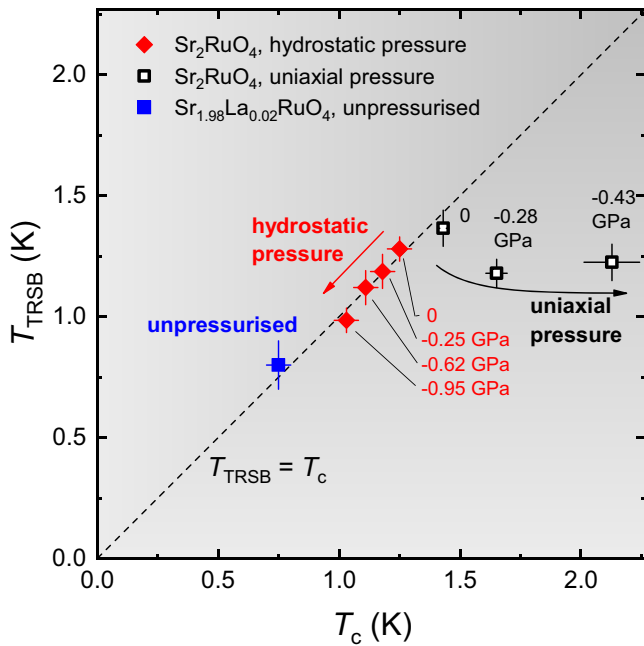


Fig. 4 Relation between T_{TRSB} and T_c . Dependence of the time reversal symmetry breaking temperature T_{TRSB} on the superconducting transition temperature T_c . The closed symbols correspond to the results obtained in present studies under hydrostatic pressure up to 0.95 GPa in pure Sr_2RuO_4 (diamonds) and in the La-doped $\text{Sr}_{2-y}\text{La}_y\text{RuO}_4$ with $T_c = 0.75(5)$ K (square). The open squares are the uniaxial pressure data for undoped Sr_2RuO_4 from ref. 47. The dashed line corresponds to $T_{\text{TRSB}} = T_c$. The minus signs at the pressure values denote the effect of ‘compression’ of the sample volume. The error bars are the same as defined in Figs. 2 and 3 and in ref. 47.

be required to obtain T_c and T_{TRSB} that split under modest uniaxial stress.

Major challenges to $d_{xz} \pm id_{yz}$ order are the absence of a resolvable second heat capacity anomaly at T_{TRSB} in measurements on uniaxially pressurised Sr_2RuO_4 ⁵², and, as already noted, the theoretical challenges in obtaining a horizontal line node in a highly two-dimensional metal⁶². We note in addition that an analysis of low-temperature thermal conductivity data indicated vertical, rather than horizontal, line nodes in Sr_2RuO_4 ⁶³. The theoretical objection to horizontal line nodes might be overcome through the complex nature of the multi-orbital band structure, including sizable spin-orbit coupling^{26,64,65}.

So we may conclude that our ZF- μSR data combined with the selection rules for ultrasound and polar Kerr effect and the NMR Knight shift behaviour are consistent with the single-representation chiral $d_{xz} + id_{yz}$ -wave state, while all composite-representation states suffer from several deficiencies. We note, however, that there are also empirical challenges to a hypothesis of $d_{xz} \pm id_{yz}$, and that the difficulty in reconciling apparently contradictory experimental results in Sr_2RuO_4 may mean that one or more major, apparently solid results will in time be found to be incorrect, either for a technical reason or in interpretation. Further experiments are therefore necessary.

Methods

$\text{Sr}_{2-y}\text{La}_y\text{RuO}_4$ single crystals. Single crystals of $\text{Sr}_{2-y}\text{La}_y\text{RuO}_4$ were grown by means of a floating zone technique³⁹. Samples for measurement under hydrostatic pressure (with $y = 0$) were cut from two rods, C140 and C171, that each grew along a $\langle 100 \rangle$ crystallographic direction. The rods have diameter $\varnothing \approx 3$ mm. Two sections of length 8–12 mm were taken from each rod. These were then cleaved, forming semi-cylindrical samples with flat surfaces perpendicular to the c -axis (see Fig. 1a).

The effect of La doping on the TRSB transition was studied on a single original $\text{Sr}_{2-y}\text{La}_y\text{RuO}_4$ crystal of length 8 mm. The La concentration was analysed by an electron-probe micro-analysis and was found to be $y \approx 0.02$. Before the μSR measurements, this rod was then cleaved into two semi-cylindrical pieces, again with the flat faces $\perp c$.

The x-ray diffraction experiments performed on small powdered pieces cut from of each particular rod gave $a = 0.3867$ nm, $c = 1.273$ nm for pure Sr_2RuO_4 and $a = 0.3865$ nm, $c = 1.274$ nm for La-substituted sample.

Specific heat of $\text{Sr}_{2-y}\text{La}_y\text{RuO}_4$ at ambient pressure. Specific heat measurements were performed at zero pressure for several pieces of $\text{Sr}_{2-y}\text{La}_y\text{RuO}_4$ single crystals, cut from the rod used for μSR measurements.

For Sr_2RuO_4 used in hydrostatic pressure measurements, the electronic specific heat capacity C_{el}/T was measured for four samples: one sample cut from each end of both the C140 and C171 sections. Results are presented in Supplementary Fig. 1 in Supplementary Note 1.

The temperature dependence of C_{el}/T for a small piece cut from the $\text{Sr}_{1.98}\text{La}_{0.02}\text{RuO}_4$ μSR sample is presented in Fig. 3b, e and Supplementary Fig. 2 in Supplementary Note 1.

μSR experiments and μSR data analysis procedure. The muon spin rotation/relaxation (μSR) experiments were performed at the μE1 and πE1 beamlines, using the GPD³⁵, and Dolly spectrometers (Paul Scherrer Institute, PSI Villigen, Switzerland). At the GPD instrument, experiments under pressure up to $p \approx 0.95$ GPa on undoped Sr_2RuO_4 were performed. At the Dolly spectrometer, measurements of $\text{Sr}_{1.98}\text{La}_{0.02}\text{RuO}_4$ at ambient pressure were conducted. At both instruments ^4He cryostats equipped with the ^3He insets (base temperature $T \approx 0.25$ K) were used.

At the GPD instrument, measurements in zero-field (ZF- μSR) and with the field applied transverse to the initial muon spin polarisation $\mathbf{P}_\mu(0)$ (TF- μSR) were performed. In two sets of ZF- μSR studies, $\mathbf{P}_\mu(0)$ was set to be parallel to the c -axis and along the ab -plane, respectively. In TF- μSR measurements the small 3 mT magnetic field was applied parallel to the c -axis and perpendicular to $\mathbf{P}_\mu(0)$.

At the Dolly instrument, in addition to ZF- and TF- μSR experiments, the LF measurements were performed. In these studies 3 mT magnetic field was applied parallel to the c -axis and to the initial muon spin polarisation $\mathbf{P}_\mu(0)$.

The experimental data were analysed by separating the μSR signal on the sample (s) and the background (bg) contributions⁶⁶:

$$A_0 P(t) = A_s P_s(t) + A_{bg} P_{bg}(t). \quad (2)$$

Here A_0 is the initial asymmetry of the muon spin ensemble, and A_s (A_{bg}) and $P_s(t)$ [$P_{bg}(t)$] are the asymmetry and the time evolution of the muon spin polarisation for muons stopped inside the sample (outside of the sample), respectively.

In a case of μSR under pressure studies, the background contribution ($\sim 50\%$ of total μSR response) is determined by the muons stopped in the pressure cell body. At ambient pressure experiment the small background contribution (of the order of 5%) is caused by muons stopped in the sample holder and the cryostat windows.

In TF- μSR experiments, the sample contribution was analysed by using the following functional form:

$$P_s^{\text{TF}}(t) = \exp\left[-\frac{\sigma^2 t^2}{2}\right] \cos(\gamma_\mu B_{\text{int}} t + \phi). \quad (3)$$

Here B_{int} is the internal field in the sample, ϕ is the initial phase of the muon spin ensemble, and $\gamma_\mu \approx 2\pi \times 135.5$ MHz/T is the muon gyromagnetic ratio. The Gaussian relaxation rate σ consists of the ‘superconducting’, σ_{sc} , and nuclear moment, σ_{nm} , contributions and it is defined as: $\sigma^2 = \sigma_{sc}^2 + \sigma_{nm}^2$. Here, σ_{sc} and σ_{nm} characterise the damping due to the formation of the flux-line lattice in the superconducting state and of the nuclear magnetic dipolar contribution, respectively. In the analysis, σ_{nm} was assumed to be constant over the entire temperature range and was fixed to the value obtained above T_c , where only nuclear magnetic moments contribute to the muon depolarisation rate (see Supplementary Fig. 3a in Supplementary Note 2).

The pressure cell contribution was described by using the following equation:

$$P_{pc}^{\text{TF}}(t) = \exp\left[-\frac{\sigma_{pc}^2 t^2}{2}\right] \cos(\gamma_\mu B_{\text{ext}} t + \phi). \quad (4)$$

Here $\sigma_{pc} \approx 0.28 \mu\text{s}^{-1}$ is the field and the temperature-independent relaxation rate of beryllium-copper³⁵, and B_{ext} is the externally applied field.

The solid lines in Fig. 2a correspond to the fit of TF- μSR data by using Eq. (2) with the sample and the background parts described by Eqs. (3) and (4). For the data presented in Fig. 3a the background contribution was described by non-relaxing function $P_{bg}^{\text{TF}}(t) = \cos(\gamma_\mu B_{\text{ext}} t + \phi)$. The good agreement between the fits and the data demonstrates that the above model describes the experimental data rather well.

With the external magnetic field applied along the crystallographic c -axis ($\mathbf{B}_{\text{ext}} \parallel c$), the superconducting contribution into the Gaussian relaxation rate σ_{sc} becomes proportional to the inverse squared in-plane magnetic penetration depth λ_{ab} ⁴². The proportionality coefficient between σ_{sc} and λ_{ab}^{-2} depends on the value of

the applied field, the symmetry of the flux-line lattice and the angular dependence of the superconducting order parameter.

The temperature dependencies of the Gaussian relaxation rate σ and the diamagnetic shift $B_{\text{int}} - B_{\text{ext}}$ are presented in Figs. 2b, c and 3b, c for Sr_2RuO_4 and $\text{Sr}_{1.98}\text{La}_{0.02}\text{RuO}_4$ samples, respectively.

In ZF and LF- μ SR experiments the sample contribution includes both, the nuclear moment relaxation and an additional exponential relaxation λ caused by appearance of spontaneous magnetic fields¹⁵:

$$P_s^{\text{ZF}}(t) = \text{GKT}_s(t) e^{-\lambda t}. \quad (5)$$

Here $\text{GKT}(t)$ is the Gaussian Kubo-Toyabe (GKT) relaxation function describing the magnetic field distribution created by the nuclear magnetic moments^{40,67}:

$$\text{GKT}(t) = \frac{1}{3} + \frac{2}{3}(1 - \sigma_{\text{GKT}}^2 t^2) e^{-\sigma_{\text{GKT}}^2 t^2/2}. \quad (6)$$

σ_{GKT} is the GKT relaxation rate.

Muons implanted in beryllium-copper pressure cell body sense solely the magnetic field distribution created by copper nuclear magnetic moments and described as:

$$P_{\text{pc}}^{\text{ZF}}(t) = \text{GKT}_{\text{pc}}(t) \quad (7)$$

with the temperature-independent relaxation rate $\sigma_{\text{GKT,BeCu}} \simeq 0.35 \mu\text{s}^{-135}$.

Fits of Eq. (2), with the sample and pressure cell parts described by Eqs. (5) and (7), to the ZF- μ SR data were performed globally. The ZF- μ SR time-spectra taken at each particular muon spin polarisation [$\mathbf{P}_\mu(0) \parallel ab$ and $\mathbf{P}_\mu(0) \parallel c$] and pressure ($p = 0.0, 0.25, 0.62$ and 0.95 GPa) were fitted simultaneously with A_s , A_{pc} , $\sigma_{\text{GKT,Sr,RuO}_4}$, $\sigma_{\text{GKT,BeCu}}$, and λ_0 as common parameters, and λ as individual parameter for each particular data set. The solid green and purple lines in Fig. 2d correspond to the fit of ZF- μ SR data by using Eq. (2) with the sample and the background parts described by Eqs. (5) and (7).

Note that the absence of strong nuclear magnetic moments in $\text{Sr}_{2-y}\text{La}_y\text{RuO}_4$ leads to the corresponding Gaussian Kubo-Toyabe relaxation rate being nearly zero. Consequently, the analysis of ZF- and LF- μ SR data for $\text{Sr}_{1.98}\text{La}_{0.02}\text{RuO}_4$ was performed by using the simple-exponential decay function:

$$P_s^{\text{ZF,LF}}(t) = e^{-\lambda t}. \quad (8)$$

The solid lines in Fig. 3d correspond to the fit of ZF- μ SR data by using Eq. (2) with the sample part described by Eq. (8) and the non-relaxing background $P_{\text{bg}}^{\text{ZF,LF}}(t) = 1$.

The temperature dependencies of the exponential relaxation rate λ are presented in Figs. 2e, f and 3e for Sr_2RuO_4 and $\text{Sr}_{1.98}\text{La}_{0.02}\text{RuO}_4$ samples, respectively.

Symmetry properties of the order parameters. Several order parameters have been proposed for the time reversal symmetry breaking superconducting state of Sr_2RuO_4 . We would like here to give a brief overview on the different options and the symmetry requirements to satisfy the selection rules for two experiments: ultrasound velocity renormalisation for the transverse c_{66} -mode and the polar Kerr effect. For tetragonal crystal symmetry with the point group D_{4h} the even parity spin-singlet pairing states can be listed according to the irreducible representations of D_{4h} , four one-dimensional ones A_{1g} , A_{2g} , B_{1g} , B_{2g} and a two-dimensional one E_u . The pair wave function $\psi_{\Gamma}(\mathbf{k})$ of the corresponding states are given by:

$$\begin{aligned} \psi_{A_{1g}}(\mathbf{k}) &= \psi_0(\mathbf{k}) & s\text{-wave} \\ \psi_{A_{2g}}(\mathbf{k}) &= \psi_0(\mathbf{k})k_x k_y (k_x^2 - k_y^2) & g_{xy(x^2-y^2)}\text{-wave} \\ \psi_{B_{1g}}(\mathbf{k}) &= \psi_0(\mathbf{k})(k_x^2 - k_y^2) & d_{x^2-y^2}\text{-wave} \\ \psi_{B_{2g}}(\mathbf{k}) &= \psi_0(\mathbf{k})k_x k_y & d_{xy}\text{-wave} \\ \psi_{E_g}(\mathbf{k}) &= \{\psi_0(\mathbf{k})k_x k_z, \psi_0(\mathbf{k})k_y k_z\} & \{d_{xz}, d_{yz}\}\text{-wave} \end{aligned} \quad (9)$$

where $\psi_0(\mathbf{k})$ is a function of \mathbf{k} invariant under all symmetry operations of the tetragonal lattice. We list here first the composite-representation TRSB states:

$$\begin{aligned} \tilde{\Gamma}_1 &= A_{1g} \oplus A_{2g} : & s + ig\text{-wave} \\ \tilde{\Gamma}_2 &= A_{1g} \oplus B_{1g} : & s + id\text{-wave} \\ \tilde{\Gamma}_3 &= A_{1g} \oplus B_{2g} : & s + id'\text{-wave} \\ \tilde{\Gamma}_4 &= B_{1g} \oplus A_{2g} : & d + ig\text{-wave} \\ \tilde{\Gamma}_5 &= B_{2g} \oplus A_{2g} : & d' + ig\text{-wave} \\ \tilde{\Gamma}_6 &= B_{1g} \oplus B_{2g} : & d + id'\text{-wave} \end{aligned} \quad (10)$$

Note that in general different representations correspond to different critical temperature. Thus, to obtain a single superconducting phase transition for the composite states an accidental degeneracy of two representations is necessary. The two states proposed so far are $\tilde{\Gamma}_2$ ^{29,30} and $\tilde{\Gamma}_4$ ^{31,32}. The two-dimensional representation allows for the combination:

$$\tilde{\Gamma}_7 = E_g : \text{chiral } d\text{-wave} \quad (11)$$

with a pair wave function $\psi_{E_g}(\mathbf{k}) = \psi_0(\mathbf{k})k_z(k_x \pm ik_y)$ as proposed in refs. ^{26,62}. All

composite states, $\tilde{\Gamma}_{1-6}$, can be constructed by electron pairing within the RuO_2 planes, while the state $\tilde{\Gamma}_7$ requires interlayer pairing. Due to the spin-singlet nature all states are compatible with the new NMR Knight shift results^{24,25}. All TRSB state are expected to generate internal spontaneous currents around defects, such as surfaces and domain walls and, consequently, under present understanding are compatible with the μ SR experiments¹⁵.

Next we consider the two selection rules. For the coupling to the lattice we restrict consideration to the mode which corresponds to the elastic constant c_{66} , which is connected with the strain tensor element $\epsilon_{xy} = \epsilon_{yx}$ ^{58,59}. This is active for transverse modes with a wave vector in the plane, e.g. [100] and a polarisation perpendicular also within the plane. This strain tensor component belongs by symmetry to the representation B_{2g} ^{58,59,68}. For the observed renormalisation of the speed of sound the superconducting order parameter has to couple linearly to ϵ_{xy} , thus, requiring that B_{2g} is contained in the decomposition of $\tilde{\Gamma}_i \otimes \tilde{\Gamma}_j$. This only possible for $\tilde{\Gamma}_3$, $\tilde{\Gamma}_4$ and $\tilde{\Gamma}_7$:

$$\tilde{\Gamma}_3 \otimes \tilde{\Gamma}_3 = \tilde{\Gamma}_4 \otimes \tilde{\Gamma}_4 = 2A_{1g} \oplus 2B_{2g} \quad (12)$$

and

$$\tilde{\Gamma}_7 \otimes \tilde{\Gamma}_7 = A_{1g} \oplus A_{2g} \oplus B_{1g} \oplus B_{2g}. \quad (13)$$

The selection rule resulting in the polar Kerr effect requires the order parameter to couple by symmetry to the z -component of the magnetic field, B_z which belongs to the representation A_{2g} . Again we consider the decomposition of the corresponding representations of the different pairing states. We find that only $\tilde{\Gamma}_1$, $\tilde{\Gamma}_6$ and $\tilde{\Gamma}_7$ satisfy the condition. The only pairing state which appears to obey both selection rules is the chiral d -wave state. None of the composite pairing states can satisfy both conditions. Among them there are the states $\tilde{\Gamma}_2$ and $\tilde{\Gamma}_5$ which are in conflict with both selection rules.

Turning to the odd parity states the analogous picture arises with:

$$\begin{aligned} d_{A_{1u}}(\mathbf{k}) &= \psi_0(\mathbf{k})(\tilde{x}k_x + \tilde{y}k_y) \\ d_{A_{2u}}(\mathbf{k}) &= \psi_0(\mathbf{k})(\tilde{x}k_x - \tilde{y}k_y) \\ d_{B_{1u}}(\mathbf{k}) &= \psi_0(\mathbf{k})(\tilde{x}k_x - \tilde{y}k_y) \\ d_{B_{2u}}(\mathbf{k}) &= \psi_0(\mathbf{k})(\tilde{x}k_x + \tilde{y}k_y) \\ d_{E_u}(\mathbf{k}) &= \psi_0(\mathbf{k})\{\tilde{z}k_x, \tilde{z}k_y\}. \end{aligned} \quad (14)$$

here listed in the convenient d -vector notation for spin-triplet pairing states (see ref. ⁶⁸). It is important to note that all composite phases from combination of two pairing states of one-dimensional representation are c -axis equal spin state and would be in agreement with present time NMR Knight data^{24,25} and had been proposed as possible states in refs. ^{69,70}. These states are also called helical state in literature, as they are topologically non-trivial with helical surface states. The Knight shift experiments disagree with expectations of the state in representation E_u which yields the chiral p -wave state.

Again we have to make composite states of the one-dimensional representation to obtain TRSB phases. Analogous to the even parity case we do not find any composite state which satisfies both selection rules, in contrast to the chiral p -wave state which behaves the same way as the chiral d -wave state in this respect.

Data availability

All data needed to evaluate the conclusions in the paper are present in the paper and/or in the Supplementary Information. Other data that support the plots within this paper and other findings of this study are available from the corresponding author upon reasonable request.

Received: 23 February 2021; Accepted: 1 June 2021;

Published online: 24 June 2021

References

- Heffner, R. H. et al. Muon-spin relaxation studies of weak magnetic correlations in $\text{U}_{1-x}\text{Th}_x\text{Be}_{13}$. *Phys. Rev. B* **40**, 806(R) (1989).
- Jin, D. S., Carter, S. A., Ellman, B., Rosenbaum, T. F. & Hinks, D. G. Uniaxial-stress anisotropy of the double superconducting transition in UPt_3 . *Phys. Rev. Lett.* **68**, 1597–1600 (1992).
- Luke, G. M. et al. Muon spin relaxation in UPt_3 . *Phys. Rev. Lett.* **71**, 1466–1469 (1993).
- Riseborough, P. & Smith, J. L. Heavy-fermion superconductivity. in *The Physics of Superconductors*, Vol II (eds Bennemann, K. H. & Ketterson, J. B.) (Springer-Verlag Berlin Heidelberg, 2002).
- Maisuradze, A. et al. Evidence for time-reversal symmetry breaking in superconducting $\text{PrPt}_4\text{Ge}_{12}$. *Phys. Rev. B* **82**, 024524 (2010).
- Hillier, A. D., Quintanilla, J., Mazidian, B., Annett, J. F. & Cywinski, R. Nonunitary triplet pairing in the centrosymmetric superconductor LaNiGa_2 . *Phys. Rev. Lett.* **109**, 097001 (2012).

7. Biswas, P. K. et al. Evidence for superconductivity with broken time-reversal symmetry in locally noncentrosymmetric SrPtAs. *Phys. Rev. B* **87**, 180503 (2013).
8. Schemm, E. R., Gannon, W. J., Wishne, C. M., Halperin, W. P. & Kapitulnik, A. Observation of broken time-reversal symmetry in the heavy-fermion superconductor UPt₃. *Science* **345**, 190–193 (2014).
9. Shang, T. et al. Time-reversal symmetry breaking in Re-based superconductors. *Phys. Rev. Lett.* **121**, 257002 (2018).
10. Ghosh, S. K. et al. Recent progress on superconductors with time-reversal symmetry breaking. *J. Phys.: Condens. Matter* **33**, 033001 (2021).
11. Grinenko, V. et al. Superconductivity with broken time-reversal symmetry inside a superconducting *s*-wave state. *Nat. Phys.* **16**, 789–794 (2020).
12. Boehm, T. et al. Balancing act: evidence for a strong subdominant d-wave pairing channel in Ba_{0.6}K_{0.4}Fe₂As₂. *Phys. Rev. X* **4**, 041046 (2014).
13. Maeno, Y. et al. Superconductivity in a layered perovskite without copper. *Nature* **372**, 532–534 (1994).
14. Mackenzie, A. P. & Maeno, Y. The superconductivity of Sr₂RuO₄ and the physics of spin-triplet pairing. *Rev. Mod. Phys.* **75**, 657–712 (2003).
15. Luke, G. M. et al. Time-reversal symmetry-breaking superconductivity in Sr₂RuO₄. *Nature* **394**, 558–561 (1998).
16. Xia, J., Maeno, Y., Beyersdorf, P. T., Fejer, M. M. & Kapitulnik, A. High resolution polar kerr effect measurements of Sr₂RuO₄: evidence for broken time-reversal symmetry in the superconducting state. *Phys. Rev. Lett.* **97**, 167002 (2006).
17. Nelson, K. D., Mao, Z. Q., Maeno, Y. & Liu, Y. Odd-parity superconductivity in Sr₂RuO₄. *Science* **306**, 1151–1154 (2004).
18. Kidwingira, F., Strand, J. D., Van Harlingen, D. J. & Maeno, Y. Dynamical superconducting order parameter domains in Sr₂RuO₄. *Science* **314**, 1267–1271 (2006).
19. Nakamura, T. et al. Essential configuration of Pb/Ru/Sr₂RuO₄ junctions exhibiting anomalous superconducting interference. *J. Phys. Soc. Jpn.* **81**, 064708 (2012).
20. Anwar, M. A. et al. Anomalous switching in Nb/Ru/Sr₂RuO₄ topological junctions by chiral domain wall motion. *Sci. Rep.* **3**, 2480 (2013).
21. Maeno, Y., Kittaka, S., Nomura, T., Yonezawa, S. & Ishida, K. Evaluation of spin-triplet superconductivity in Sr₂RuO₄. *J. Phys. Soc. Jpn.* **81**, 011009 (2012).
22. Yonezawa, S., Kajikawa, T. & Maeno, Y. First-order superconducting transition of Sr₂RuO₄. *Phys. Rev. Lett.* **110**, 077003 (2013).
23. Kittaka, S. et al. Sharp magnetization jump at the first-order superconducting transition in Sr₂RuO₄. *Phys. Rev. B* **90**, 220502 (2014).
24. Pustogow, A. et al. Constraints on the superconducting order parameter in Sr₂RuO₄ from oxygen-17 nuclear magnetic resonance. *Nature* **574**, 72–75 (2019).
25. Ishida, K., Manago, M. & Maeno, Y. Reduction of the ¹⁷O knight shift in the superconducting state and the heat-up effect by NMR pulses on Sr₂RuO₄. *J. Phys. Soc. Jpn.* **89**, 034712 (2020).
26. Suh, H. G. et al. Stabilizing even-parity chiral superconductivity in Sr₂RuO₄. *Phys. Rev. Res.* **2**, 032023(R) (2020).
27. Kasahara, Y. et al. Exotic superconducting properties in the electron-hole-compensated heavy-fermion 'Semimetal' URu₂Si₂. *Phys. Rev. Lett.* **99**, 116402 (2007).
28. Schemm, E. R. et al. Evidence for broken time-reversal symmetry in the superconducting phase of URu₂Si₂. *Phys. Rev. B* **91**, 140506(R) (2015).
29. Römer, A. T., Scherer, D. D., Eremin, I. M., Hirschfeld, P. J. & Andersen, B. M. Knight shift and leading superconducting instability from spin fluctuations in Sr₂RuO₄. *Phys. Rev. Lett.* **123**, 247001 (2019).
30. Römer, A. T. et al. Theory of strain-induced magnetic order and splitting of *T_c* and *T_{TRSB}* in Sr₂RuO₄. *Phys. Rev. B* **102**, 054506 (2020).
31. Kivelson, S. A., Yuan, A. C., Ramshaw, B. & Thomale, R. A proposal for reconciling diverse experiments on the superconducting state in Sr₂RuO₄. *npj Quantum Mat.* **5**, 43 (2020).
32. Willa, R. Symmetry-mixed bound-state order. *Phys. Rev. B* **102**, 180503(R) (2020).
33. Zinkl, B. & Sigrist, M. Impurity induced double transitions for accidentally degenerate unconventional pairing states. *Phys. Rev. Research* **3**, L012004 (2021).
34. Andreica, D. *Magnetic Phase Diagram in Some Kondo-lattice Compounds*. PhD thesis, ETH Zürich (2001).
35. Khasanov, R. et al. High pressure research using muons at the Paul Scherrer Institute. *High Pressure Res.* **36**, 140–166 (2016).
36. Sheradini, Z. et al. A low-background piston cylinder-type hybrid high pressure cell for muon-spin rotation/relaxation experiments. *High Pressure Res.* **37**, 449–464 (2017).
37. Murata, K., Yoshino, H., Yadav, H. O., Honda, Y. & Shirakawa, N. Pt resistor thermometry and pressure calibration in a clamped pressure cell with the medium, Daphne 7373. *Rev. Sci. Instrum.* **68**, 2490–2493 (1997).
38. Steppke, A. et al. Strong peak in *T_c* of Sr₂RuO₄ under uniaxial pressure. *Science* **355**, eaaf9398 (2017).
39. Bobowski, J. S. et al. Improved single-crystal growth of Sr₂RuO₄. *Condens. Matter* **4**, 6 (2019).
40. Yaouanc, A. & Dalmas de Réotier, P. *Muon Spin Rotation, Relaxation and Resonance: Applications to Condensed Matter* (Oxford University Press, 2011).
41. Weber, M. et al. Magnetic-flux distribution and the magnetic penetration depth in superconducting polycrystalline Bi₂Sr₂Ca_{1-x}Y_xCu₂O_{8+δ} and Bi_{2-x}Pb_xSr₂CaCu₂O_{8+δ}. *Phys. Rev. B* **48**, 13022 (1993).
42. Khasanov, R. et al. Proximity-induced superconductivity within the insulating (Li_{0.84}Fe_{0.16})OH layers in (Li_{0.84}Fe_{0.16})OHFe_{0.98}Se. *Phys. Rev. B* **93**, 224512 (2016).
43. Shirakawa, N., Murata, K., Nishizaki, S., Maeno, Y. & Fujita, T. Pressure dependence of superconducting critical temperature of Sr₂RuO₄. *Phys. Rev. B* **56**, 7890 (1997).
44. Forsythe, D. et al. Evolution of fermi-liquid interactions in Sr₂RuO₄ under pressure. *Phys. Rev. Lett.* **89**, 166402 (2002).
45. Svitskiy, O. et al. Influence of hydrostatic pressure on the magnetic phase diagram of superconducting Sr₂RuO₄ by ultrasonic attenuation. *Phys. Rev. B* **77**, 052502 (2008).
46. Luke, G. M. et al. Unconventional superconductivity in Sr₂RuO₄. *Physica B* **289-290**, 373–376 (2000).
47. Grinenko, V. et al. Split superconducting and time-reversal symmetry-breaking transitions, and magnetic order in Sr₂RuO₄ under stress. *Nat. Phys.* <https://doi.org/10.1038/s41567-021-01182-7> (2021).
48. Shiroka, T. et al. μ SR studies of superconductivity in eutectically grown mixed ruthenates. *Phys. Rev. B* **85**, 134527 (2012).
49. Higemoto, W., Koda, A., Kadono, R., Yoshida, Y. & Onuki, Y. Investigation of spontaneous magnetic field in spin-triplet superconductor Sr₂RuO₄. *JPS Conf. Proc.* **2**, 010202 (2014).
50. Kikugawa, N. et al. Rigid-band shift of the Fermi level in the strongly correlated metal: Sr_{2-y}La_yRuO₄. *Phys. Rev. B* **70**, 060508(R) (2004).
51. Shen, K. M. et al. Evolution of the fermi surface and quasiparticle renormalization through a van Hove singularity in Sr_{2-y}La_yRuO₄. *Phys. Rev. Lett.* **99**, 187001 (2007).
52. Li, Y.-S. et al. High sensitivity heat capacity measurements on Sr₂RuO₄ under uniaxial pressure. *PNAS* **118**, e2020492118 (2021).
53. Bud'ko, S. L., Ni, N. & Canfield, P. C. Jump in specific heat at the superconducting transition temperature in Ba(Fe_{1-x}Co_x)₂As₂ and Ba(Fe_{1-x}Ni_x)₂As₂ single crystals. *Phys. Rev. B* **79**, 220516(R) (2009).
54. Kirtley, J. R. et al. Upper limit on spontaneous supercurrents in Sr₂RuO₄. *Phys. Rev. B* **76**, 014526 (2007).
55. Curran, P. J. et al. Search for spontaneous edge currents and vortex imaging in Sr₂RuO₄ mesostructures. *Phys. Rev. B* **89**, 144504 (2014).
56. Ghosh, S. et al. Thermodynamic evidence for a two-component superconducting order parameter in Sr₂RuO₄. *Nat. Phys.* **17**, 199–204 (2021).
57. Benhabib, S. et al. Ultrasound evidence for a two-component superconducting order parameter in Sr₂RuO₄. *Nat. Phys.* **17**, 194–198 (2021).
58. Walker, M. B. & Contreras, P. Theory of elastic properties of Sr₂RuO₄ at the superconducting transition temperature. *Phys. Rev. B* **66**, 214508 (2002).
59. Sigrist, M. Ehrenfest relations for ultrasound absorption in Sr₂RuO₄. *Progress of Theoretical Physics* **107**, 917–925 (2002).
60. Römer, A. T., Hirschfeld, P. J. & Andersen, B. M. Superconducting state of Sr₂RuO₄ in the presence of longer-range Coulomb interactions. Preprint at <https://arxiv.org/abs/2101.06972> (2021).
61. Willa, R., Hecker, M., Fernandes, R. M. & Schmalian, J. Inhomogeneous time-reversal symmetry breaking in Sr₂RuO₄. Preprint at <https://arxiv.org/abs/2011.01941> (2021).
62. Zutic, I. & Mazin, I. Phase-sensitive tests of the pairing state symmetry in Sr₂RuO₄. *Phys. Rev. Lett.* **95**, 217004 (2005).
63. Hassinger, E. et al. Vertical line nodes in the superconducting gap structure of Sr₂RuO₄. *Phys. Rev. X* **7**, 011032 (2017).
64. Gingras, O., Nourafkan, R., Tremblay, A.-M. S. & Côté, M. Superconducting symmetries of Sr₂RuO₄ from first-principles electronic structure. *Phys. Rev. Lett.* **123**, 217005 (2019).
65. Puetter, C. M. & Kee, H.-Y. Identifying spin-triplet pairing in spin-orbit coupled multi-band superconductors. *Europhys. Lett.* **98**, 27010 (2012).
66. Khasanov, R. et al. Pressure-induced electronic phase separation of magnetism and superconductivity in CrAs. *Sci. Rep.* **5**, 13788 (2015).
67. Hayano, R. S. et al. Zero- and low-field spin relaxation studied by positive muons. *Phys. Rev. B* **20**, 850–859 (1979).
68. Sigrist, M. & Ueda, K. Phenomenological theory of unconventional superconductivity. *Rev. Mod. Phys.* **63**, 239–311 (1991).
69. Kashiwaya, S. et al. Time-reversal invariant superconductivity of Sr₂RuO₄ revealed by Josephson effects. *Phys. Rev. B* **100**, 094530 (2019).
70. Ikegaya, S. et al. Identification of spin-triplet superconductivity through a helical-chiral phase transition in Sr₂RuO₄ thin-films. *Phys. Rev. B* **101**, 220501 (2020).
71. Hatlo, M. et al. Developments of mathematical software libraries for the LHC experiments. *IEEE Trans. Nucl. Sci.* **52**, 2818–2822 (2005).

Acknowledgements

The work was performed at the Swiss Muon Source ($S\mu S$), Paul Scherrer Institute (PSI, Switzerland). We acknowledge fruitful discussions with Zurab Guguchia, Carsten Timm and Jing Xia. Matthias Elender is acknowledged for technical support. The work of R.G. is supported by the Swiss National Science Foundation (SNF Grant No. 200021-175935). The work of M.S. and B.Z. was financially supported by the Swiss National Science Foundation (SNSF) through Division II (Grant No. 184739). The work of V.G. was supported by DFG GR 4667/1. N.K. acknowledges the support from JSPS KAKENHI (Nos. JP18K04715, and JP21H01033) in Japan. Y.M. acknowledges funding by JPJS-CNR-SPIN Core-to-core programme (No. JPJSCCA20170002), and by JPJS KAKENHI Nos. JP15H05852, JP15K21717, and JP17H06136. The work of H.-H.K. was supported by DFG SFB 1143 and GRK 1621.

Author contributions

R.K., V.G. and M.S. conceived the project. Data were taken by R.K., V.G., D.D. and R.G. R.K. and V.G. performed data analysis and interpreted the results together with M.S. B.Z. and M.S. provided the theoretical analysis. N.K. provided and characterised samples. R.K., V.G., M.S. and C.W.H. wrote the manuscript with inputs from all authors: D.D., R.G., B.Z., N.K., Y.M. and H.-H.K.

Competing interests

The authors declare no competing interests.

Additional information

Supplementary information The online version contains supplementary material available at <https://doi.org/10.1038/s41467-021-24176-8>.

Correspondence and requests for materials should be addressed to V.G., M.S. or R.K.

Peer review information *Nature Communications* thanks Amit Keren and the other, anonymous, reviewer(s) for their contribution to the peer review of this work. Peer reviewer reports are available.

Reprints and permission information is available at <http://www.nature.com/reprints>

Publisher's note Springer Nature remains neutral with regard to jurisdictional claims in published maps and institutional affiliations.



Open Access This article is licensed under a Creative Commons Attribution 4.0 International License, which permits use, sharing, adaptation, distribution and reproduction in any medium or format, as long as you give appropriate credit to the original author(s) and the source, provide a link to the Creative Commons license, and indicate if changes were made. The images or other third party material in this article are included in the article's Creative Commons license, unless indicated otherwise in a credit line to the material. If material is not included in the article's Creative Commons license and your intended use is not permitted by statutory regulation or exceeds the permitted use, you will need to obtain permission directly from the copyright holder. To view a copy of this license, visit <http://creativecommons.org/licenses/by/4.0/>.

© The Author(s) 2021